

# Dissecting strong-field excitation dynamics with atomic-momentum spectroscopy

A.W. Bray,<sup>1,\*</sup> U. Eichmann,<sup>2,†</sup> and S. Patchkovskii<sup>2,‡</sup>

<sup>1</sup>*Australian National University, Canberra*

<sup>2</sup>*Max-Born-Institute, Berlin, Germany*

(Dated: December 5, 2021)

Strong, focussed linearly-polarized infra-red fields electronically excite and accelerate atoms in the laser propagation and the transverse directions. We develop a numerically-tractable, quantum-mechanical treatment of correlations between internal and centre-of-mass (c.m.) dynamics, and apply it to the hydrogen atom. The propagation-direction c.m. momentum carries no information on the internal dynamics. The transverse momentum records the time spent in the field, allowing femtosecond reconstruction of the strong-field excitation process. The ground state becomes weak-field seeking, an unambiguous signature of the Kramers-Henneberger regime.

The seminal strong-field ionization concept[1] together with the notion of field-induced electronic recollisions[2] have laid the foundation for a thorough understanding of strong-field processes in atomic and molecular science. The fundamental importance of non-dipole effects have been recognized early on[3–5], but only recently, enabled by refined theoretical and experimental approaches, processes beyond the dipole-approximation have come into focus. These include radiation pressure[6], momentum distribution between fragments upon ionization[7–9], and chiral effects in HHG[10]. The effects have been investigated for very intense (relativistic and near-relativistic) infra-red (IR) fields[11–14], as well as for shorter-wavelength fields which are becoming available in the strong-field regime[15].

One of the more intriguing non-dipole effects of strong laser field is its ability to accelerate neutral atoms and molecules[16–21], with peak accelerations potentially exceeding  $10^{14}$  g[16]. This acceleration is closely connected to the strong-field excitation of high Rydberg states[22, 23]. Under favourable conditions, a few percent of the initially-present atoms may be left in such states[22, 24–28], with the population of the individual levels being a complex function of the wavelength, peak intensity, and the field envelope[27, 29–31]. Because high-Rydberg states generally exhibit large, negative free-electron-like dynamical polarizabilities, they are low-field-seeking, and are expelled from the centre of the laser beam[23]. For atoms initially close to the beam waist, this ponderomotive acceleration is preferentially in a direction transverse to the beam propagation direction. Furthermore, energy exchange between the atom and the field is necessarily accompanied by the transfer of momentum. The latter acceleration due to the radiation pressure is in the beam-propagation direction.

Combined with the rich and complex strong-field excitation dynamics, the two acceleration mechanisms lead to highly-structured final atomic-velocity distributions, which are thus far poorly understood. The goal of this Letter is to explore theoretically the relationship between the final internal state of an atom and its c.m. momentum in a strong, non-uniform IR field, and to motivate

its experimental investigation. To this end, we develop a numerically-tractable treatment of correlations between the internal and c.m. degrees of freedom, going beyond the usual separation of the c.m. coordinates. We further show that the c.m.-momentum spectroscopy records strong-field excitation dynamics and monitors formation of Kramers-Henneberger states[19, 32–39].

In the simplest case of a 1-electron, neutral atom, the laboratory-frame Hamiltonian is given by (unless noted otherwise, atomic units ( $\hbar = m = |e| = 1$ ) are used throughout):

$$\hat{H} = \frac{1}{2m_1} \left( \hat{p}_1 + \vec{A}(\vec{r}_1, t) \right)^2 + \frac{1}{2m_2} \left( \hat{p}_2 - \vec{A}(\vec{r}_2, t) \right)^2 + v(\vec{\chi}) + u(\vec{R}) \quad (1)$$

where  $\hat{p}_{1,2}$  are the momentum operators of particles 1 (electron, charge  $q_1=-1$ ) and 2 (nucleus,  $q_2=+1$ ),  $\vec{A}(\vec{r}, t)$  is the transverse ( $\hat{\nabla} \cdot \vec{A} = 0$ ) laboratory-space vector-potential,  $v(\vec{\chi})$  is the interaction potential between the particles, and  $u(\vec{R})$  is the c.m. trapping potential (in free space,  $u=0$ ). The variables  $\vec{\chi}$  and  $\vec{R}$  are given by:

$$\vec{\chi} = \vec{r}_1 - \vec{r}_2 \quad (2)$$

$$\vec{R} = (m_1/M)\vec{r}_1 + (m_2/M)\vec{r}_2 \quad (3)$$

where  $M=m_1+m_2$ . For systems of interest here,  $m_1 \ll m_2$ . Introducing  $\mu=m_1m_2/M$  and neglecting correction terms of the order  $O(\mu/M)$  in the laser interaction, Eq. (1) simplifies to:

$$\hat{H}_{\text{CoM}} = \hat{H}_\chi + \hat{H}_R \quad (4)$$

$$\hat{H}_\chi = \frac{1}{2\mu} \left( \hat{p}_\chi + \vec{A}(\vec{R} + \vec{\chi}, t) \right)^2 + v(\vec{\chi}) \quad (5)$$

$$\hat{H}_R = \frac{1}{2M} \hat{p}_R^2 + u(\vec{R}) . \quad (6)$$

No field-coupling term is associated with  $\hat{p}_R$  in this order. We have verified that the terms omitted in Eq. (4) do not affect the results reported below[40].

The general-case treatment of Eq. (4), which contains a non-separable coupling term through  $\vec{A}(\vec{R} + \vec{\chi}, t)$ ,

remains a formidable numerical task. For the short (sub-picosecond) and moderately-intense IR fields, the c.m. displacements remain small compared to both the characteristic electron excursion and the laser-field wavelength. We therefore seek solutions of the time-dependent Schrödinger equation (TDSE) in the close-coupling form:

$$\Psi(\vec{\chi}, \vec{R}, t) = \sum_n \phi_n(\vec{\chi}, t) \zeta_n(\vec{R}) \quad (7)$$

(From now on, we will omit arguments of  $\phi_n$ ,  $\zeta_n$  and other spatially- and time-dependent quantities, as long as their choice is unambiguous.) In Eq. (7), functions  $\zeta_n$  are orthonormalized, time-independent eigenfunctions of  $\hat{H}_R$  (Eq. (6)) with eigenvalues  $\epsilon_n$ . We assume that the potential  $u(\vec{R})$  in Eq. (6) is such that the set of the discrete solutions  $\{\zeta_n\}$  is complete.

Substituting the Ansatz (7) into the TDSE for the Hamiltonian (4) and projecting on each  $\zeta_m$  on the left, we obtain:

$$i \frac{\partial}{\partial t} \phi_m = (\hat{h} + \epsilon_m) \phi_m + \sum_n \hat{h}_{mn} \phi_n \quad (8)$$

$$\hat{h} = \frac{1}{2\mu} \hat{p}_\chi^2 + v + \frac{1}{\mu} \vec{A} \cdot \hat{p}_\chi + \frac{1}{2\mu} A^2 \quad (9)$$

$$\hat{h}_{mn} = \vec{\eta}_{mn} \cdot \hat{p}_\chi + \kappa_{mn} \quad (10)$$

$$\vec{\eta}_{mn} = \frac{1}{\mu} \sum_{b=x,y,z} \vec{A}^{(b)} \langle \zeta_m | R_b | \zeta_n \rangle \quad (11)$$

$$\begin{aligned} \kappa_{mn} = & \frac{1}{2\mu} \sum_{b=x,y,z} \left( \frac{\partial}{\partial \chi_b} A^2 \right) \langle \zeta_m | R_b | \zeta_n \rangle \\ & + \frac{1}{2\mu} \sum_{b,c=x,y,z} \vec{A}^{(b)} \cdot \vec{A}^{(c)} \langle \zeta_m | R_b R_c | \zeta_n \rangle. \end{aligned} \quad (12)$$

In Eqs. (8)–(12),  $\vec{A}$  and  $\vec{A}^{(b)}$  are functions of the inter-particle distance  $\vec{\chi}$  and time  $t$ . We further assume that the higher-order terms in the Taylor expansion for the c.m. coordinate:

$$\vec{A}(\vec{R} + \vec{\chi}, t) = \vec{A}(\vec{\chi}, t) + \sum_{a=x,y,z} \vec{A}^{(a)}(\vec{\chi}, t) R_a + \dots \quad (13)$$

can be neglected.

The system of coupled PDEs (8) can be propagated in time at a cost comparable to that of a standard, fixed-nuclei electronic TDSE, provided that the number of the nuclear-coordinate channels is not excessive. At the end of the pulse, the expectation of a c.m. observable  $\hat{O}$ , conditional on the internal degree of freedom being described by a normalized wavefunction  $\phi_f(\chi)$ , is given by:

$$\langle O \rangle_f = \sum_{mn} \langle \zeta_m | \hat{O} | \zeta_n \rangle \langle \phi_m | \phi_f \rangle \langle \phi_f | \phi_n \rangle. \quad (14)$$

Choosing  $\hat{O} = \hat{p}_R$  and  $\hat{O} = \hat{1}$  yields the expectation of the momentum and the state population, respectively. The c.m. velocity of the atom in an internal state  $\phi_f$  is then:

$$v_f = \frac{1}{M} \frac{\langle p_R \rangle_f}{\langle 1 \rangle_f}. \quad (15)$$

We solve Eq. (8) for a 3-dimensional hydrogen atom ( $\mu = 1$ ,  $M = 1836$ ), initially in the  $1s$  electronic ground state, exposed to a Gaussian pulse of beam waist  $w_0 = 30236 a_0$ , central frequency  $\omega = 0.057$  ( $\lambda \approx 799$  nm), and full-width-half-maximum  $\tau_0 = 220$  ( $\approx 5.32$  fs). We choose for each Cartesian direction the following convention:  $x$ –beam propagation,  $y$ –transverse, and  $z$ –polarization. For further details of the numerical parameters please see[40].

In a spatially non-uniform laser field, the excited atoms acquire the velocity both in the forward and in the transverse directions. The final c.m. velocity along laser polarization remains negligible, as required by symmetry. We have verified numerically that the forward velocity is insensitive to moderate spatial-intensity gradients. As a result, we discuss the two components of the velocity independently.

The forward (propagation-direction) component of velocity can be understood as the consequence of the radiation pressure. Strong-field excitation between hydrogenic levels with the principal quantum numbers  $n$  and  $n'$  transfers the energy of  $\Delta E = 0.5(n^{-2} - n'^{-2})$  from the laser field to the atom. The corresponding momentum transfer is  $\Delta E/c$ , giving the velocity:

$$\Delta v_f = \frac{\Delta E}{Mc}. \quad (16)$$

Because the forward velocity is determined solely by the initial and the final internal state of the atom, it contains no information on the intervening dynamics. Our numerical results (See Figs. S1, S2[40]) are consistent with these expectations. Therefore, we will not discuss the forward component of the velocity any further.

In the transverse direction the atoms are accelerated by the spatial gradient of the ponderomotive potential. Classically, the final outward velocity of an initially-stationary particle with dipole polarizability  $\alpha$  entering the field at time  $t_0$  in the vicinity of the beam waist ( $x=0$ , Eq. (S1)) is given by:

$$\Delta v_t = \frac{\alpha}{2M} \int_{t_0}^{\infty} \frac{\partial}{\partial r} F^2(r, t) dt \quad (17)$$

where  $F(r, t) = -\frac{\partial}{\partial t} A(r, t)$  is laser electric field (see Eq. (S1)). The hydrogen ground state ( $\alpha_0 = 4.5$ ) is expected to be accelerated towards stronger fields ( $\frac{\partial}{\partial r} F_0^2 < 0$ ). Conversely, high-Rydberg states, which exhibit the free-electron-like dynamical polarizabilities in low-frequency fields ( $\alpha_f \approx -\omega^{-2} \approx -308$  at 799 nm),

are expected to move towards weaker fields. Because  $|\alpha_f| \gg |\alpha_0|$ , Rydberg states are also expected to reach much higher final velocities.

A comparison of the calculated transverse velocity (Eq. (15)) with the classical Eq. (17) for a state a known polarizability allows us to infer  $t_b$  — the time this state has entered the field. The integrand in Eq. (17) is negative, so that  $\Delta v_t$  is a monotonous function of  $t_b$ . Because  $\alpha_f$ , the low-frequency dynamical polarizability of the Rydberg states, is a cycle-averaged quantity, the clock defined by the Eq. (17) offers no meaningful sub-cycle resolution.

The composition of the Rydberg states populated by strong-field excitation is sensitively affected by channel closings[27, 30, 31]. We therefore expect a similar effect to arise in the c.m. velocity spectroscopy. At 799 nm, channel closings occur each  $26 \text{ TW cm}^{-2}$  ( $\Delta I_{\text{channel}} = 4\omega^3$ ). For a tightly-focussed beam used presently ( $w_0 = 2\lambda$ ), in the vicinity of the beam half-waist a channel closing occurs each  $648 a_0$ , or  $\approx 34 \text{ nm}$ . We consider the channel-closing effects by repeating the calculations at seven, equidistant transverse points spaced by  $216 a_0$ , placed around the beam half-waist. We average the results equally among these points. This volume averaging effectively suppresses resonance contributions, which are highly sensitive to the intensity (See [40]).

The maximum of the spatial gradient of the ponderomotive potential is found on a ring of the radius  $w_0/2$  around the focal spot, normal to the beam propagation direction. Accordingly we choose the point displaced in the  $y$  direction, perpendicular to both the propagation and polarization directions. The volume-averaged numerical results at this point are illustrated in Fig. 1. The non-paraxial field contributions (see Eq. (S2)) vanish in the vicinity of this point, simplifying the analysis. The local peak intensity of the field is  $\approx 607 \text{ TW cm}^{-2}$ . The ionization is in the saturation regime, with  $\approx 9\%$  of the population surviving in the  $1s$  ground state after the pulse. Additionally,  $\approx 2.4\%$  of the atoms are excited to Rydberg states with  $n \leq 6$ . Although our simulation volume does not allow an accurate determination of excitation probabilities for higher Rydberg states, we estimate that at least 2% of the atoms are left in Rydberg states with  $n \geq 7$ . Most of the excited states possess magnetic quantum number  $m = 0$ , same as the initial state. However, due to the presence of the magnetic-field component, states with  $m \neq 0$  are also populated. The final populations of  $m = \pm 1$  and  $m = \pm 2$  manifolds are 4 and 8 orders of magnitude below the  $m = 0$  populations with the same principal quantum number  $n$ , consistent with the expected lowest-order magnetic-transition probabilities.

For all electronic states in Fig. 1c other than the ground state, the final transverse velocities are in the range of  $12\text{--}20 \text{ m s}^{-1}$ . Assuming the free-electron-like polarizability, solving Eq. (17) for  $t_b$  yields the excita-

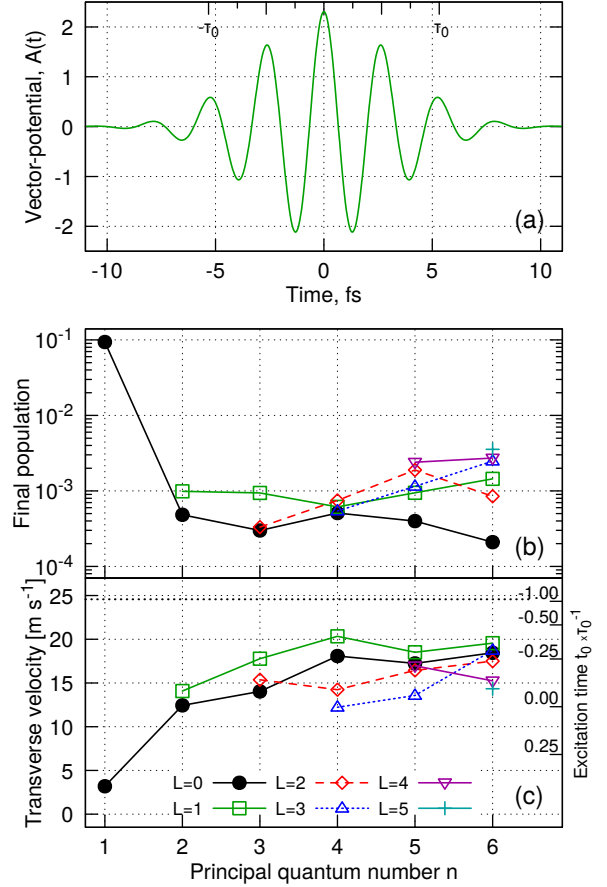


FIG. 1. (Color online) Hydrogen atom initially at the half-waist position. The results are volume-averaged about the Cartesian point  $(0, w_0/2 \pm 648, 0)$ . The local peak intensity is  $\approx 607 \text{ TW cm}^{-2}$ . (a) Vector-potential at the initial position as a function of time. The upper horizontal axis gives the fraction of the pulse duration  $\tau_0$ . (b) Population of the individual  $m=0$  bound states after the end of the pulse. (c) Final c.m. velocity in the outward transverse direction in meters per second ( $1 \approx 2.19 \times 10^6 \text{ m s}^{-1}$ ). The right vertical axis gives the time when a particle with free-electron polarizability needs to enter the field to reach the observed transverse velocity (Eq. (17)). Final velocities above the dotted horizontal line cannot be reached by a free-electron-like particle. The connecting lines in panels (b,c) are only a guide for the eye.

tion time. The results for the volume-averaged excitation time reconstruction are presented in Fig. 2. In nearly all cases, excited states are formed before the peak of the envelope, with two main clusters at approximately  $-0.7$  ( $2p, 3s, 3d, 4d, 5s, 5d, 5f, 5g, 6d, 6g$ , and  $6h$ ) and  $-1.7$  fs ( $3p, 4s, 4p, 5p, 6s, 6p, 6f$ ). Interestingly, both clusters gravitate towards the zeros of the vector-potential, near the peaks of the electric field. These times of birth are consistent with the expectations from the semi-classical frustrated tunneling model[22]. Intriguingly, two of the excited states ( $2s$  and  $4f$ ) appear to be preferentially formed near the peak of the vector-potential, respectively at  $-0.2$  and  $+0.2$  fs. These times of birth, and the broad

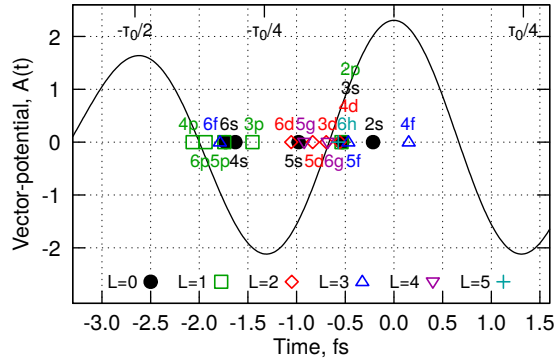


FIG. 2. (Color online) Reconstructed excitation times for the c.m. velocity spectra averaged over  $\pm 648 a_0$  about the half-waist position (See text and Fig. 1 for the raw data). The vector potential at the Cartesian point  $(0, w_0/2, 0)$  is given by the black solid line. Peak of the envelope is at the time zero.

spread of the times of birth within the two clusters in Fig. 2 would seem to indicate that the multi-photon excitation mechanism is also active. This observation is consistent with the value of the Keldysh parameter  $\gamma \approx 0.4$  ( $\gamma = \sqrt{\Delta E/2U_p}$ ), indicating dynamics in a regime intermediate between tunneling and multi-photon transitions.

We present further fixed-intensity results (Figs. S1–S3), and explore the effects of the carrier-envelope phase (CEP, Figs. S4, S5), pulse duration (Figs. S6, S7), and non-paraxial effects arising in a tightly-focussed beam (Figs. S8, S9) in [40]. In all cases, we can successfully assign the preferred excitation times based on the volume-averaged c.m.-velocity spectra, confirming that the technique is universally applicable and experimentally realizable. With a few exceptions, the reconstructed excitation times fall before the peak of the envelope, and tend to cluster around the zeros of the vector-potential.

Because the present ponderomotive clock is not sub-cycle accurate, the preference for the peak electric field (zeros of the vector-potential) should be taken as an inkling of the possible future developments. It might be possible to improve the time resolution of the excitation clock using multi-colour techniques, which have been successful for the reconstruction of the ionization and recollision times in high-harmonic spectroscopy[41, 42]. Another possibility involves breaking the symmetry of the interaction with a static, external magnetic field. Both possibilities are currently under investigation.

One remarkable result seen in Fig. 1c, which so far has not been remarked upon, is the behaviour of the 1s ground state. For the laser pulse in Fig. 1a, it is *weak-field* seeking, reaching the final outward velocity of  $\approx 3.2 \text{ m s}^{-1}$ . The low-field-seeking behaviour of the 1s state persists for other field parameters as well, with it reaching respectively 3.3, 5.2, and  $3.2 \text{ m s}^{-1}$  outward velocity for the pulse with the sine CEP (Fig. S4), 10.6 fs duration (Fig. S6), and in the presence of non-paraxial

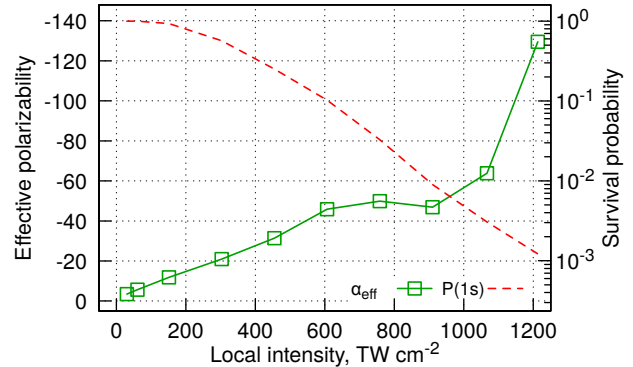


FIG. 3. (Color online) Effective polarizability  $\alpha_{\text{eff}}$  (green solid line; left vertical axis) and survival probability (red dashed line; right vertical axis) of the 1s ground state. The spatio-temporal field profile is the same as in Fig. 1. The peak intensity  $I_0$  varies from  $50 \text{ TW cm}^{-2}$  to  $2 \text{ PW cm}^{-2}$ . The horizontal axis shows the local peak intensity at the initial, half-waist position of the atom ( $I_{\text{loc}} \approx 0.607 \times I_0$ ). The results are not volume-averaged, see text.

effects (Fig. S8). The final 1s velocity is also insensitive to channel-closing effects, indicating that it arises due to adiabatic modification of the ground state, rather than transient population of high-Rydberg states.

Because the 1s state existed before the arrival of the pulse,  $t_b \rightarrow -\infty$ , and Eq. (17) can be solved for the effective polarizability  $\alpha_{\text{eff}}$ . We have explored  $\alpha_{\text{eff}}$  as a function of the peak intensity of the laser pulse, for the same spatio-temporal pulse profile as used in Fig. 1. The results for  $I_0$  in the range of  $50 \text{ TW cm}^{-2}$  to  $2 \text{ PW cm}^{-2}$  are collected in Fig. 3. At lower intensities, the numerical accuracy is insufficient to determine the final c.m. velocity (see Fig. S10[40]), while at higher intensities the survival probability becomes too low. In the entire range of the intensities, the effective polarizability is negative, as opposed to  $+4.5$  expected for 1s in a weak field. At higher intensities, the effective polarizability becomes comparable to the free-electron value ( $\approx -308$  at this laser frequency). This indicates a remarkable, field-induced modification of the electronic structure of the ground state. This modification is characteristic of entering the Kramers-Henneberger regime[19]. Observation of Kramers-Henneberger regime for an atomic ground state in strong, low-frequency fields has been long sought after, with no unambiguous detection thus far[19].

To summarize, we have developed a computationally-tractable quantum mechanical approach to correlations between c.m. motion and internal electronic dynamics in strong, non-uniform laser fields. Using the technique, we demonstrate that the final c.m. velocity is sensitive to the internal excitation dynamics. In particular the transverse, ponderomotive velocity is determined by the total time the excited state spends in the field. In the absence of resonances, it yields a measurement of the preferential time of excitation. This procedure is robust to limited

volume averaging, and can be applied for different CEP values, for longer pulses, and for non-paraxial beams. Finally, we demonstrate an unambiguous signature of the atomic ground state entering the Kramers-Henneberger regime in strong, low-frequency fields, which has been long sought-for. Taken together, our results suggest that c.m.-velocity spectroscopy is a powerful, and so far overlooked tool for understanding strong-field bound-state electronic dynamics on their natural timescale.

\* alexander.bray@anu.edu.au

† eichmann@mbi-berlin.de

‡ sergei.patchkovskii@mbi-berlin.de

- [1] L. V. Keldysh, “Ionization in the field of a strong electromagnetic wave,” Sov. Phys. JETP **20**, 1307 (1965).
- [2] P. B. Corkum, “Plasma perspective on strong field multiphoton ionization,” Phys. Rev. Lett. **71**, 1994–1997 (1993).
- [3] H. R. Reiss, “Complete Keldysh theory and its limiting cases,” Phys. Rev. A **42**, 1476–1486 (1990).
- [4] C. C. Chirilă and M. Lein, “Effect of dressing on high-order harmonic generation in vibrating H<sub>2</sub> molecules,” Phys. Rev. A **77**, 043403 (2008).
- [5] H. R. Reiss, “Limits on tunneling theories of strong-field ionization,” Phys. Rev. Lett. **101**, 043002 (2008).
- [6] A. Ludwig, J. Maurer, B. W. Mayer, C. R. Phillips, L. Gallmann, and U. Keller, “Breakdown of the dipole approximation in strong-field ionization,” Phys. Rev. Lett. **113**, 243001 (2014).
- [7] C. T. L. Smeenk, L. Arissian, B. Zhou, A. Mysyrowicz, D. M. Villeneuve, A. Staudte, and P. B. Corkum, “Partitioning of the linear photon momentum in multiphoton ionization,” Phys. Rev. Lett. **106**, 193002 (2011).
- [8] Szczenep Chelkowski, André D. Bandrauk, and Paul B. Corkum, “Photon momentum sharing between an electron and an ion in photoionization: From one-photon (photoelectric effect) to multiphoton absorption,” Phys. Rev. Lett. **113**, 263005 (2014).
- [9] A. Hartung, S. Eckart, S. Brennecke, J. Rist, D. Trabert, K. Fehre, M. Richter, H. Sann, S. Zeller, K. Henrichs, G. Kastirke, J. Hoehl, A. Kalinin, M. S. Schöffler, T. Jahnke, L. Ph H. Schmidt, M. Lein, M. Kunitski, and R. Dörner, “Magnetic fields alter strong-field ionization,” Nature Physics **15**, 1222–1226 (2019).
- [10] R. Cireasa, A. E. Boguslavskiy, B. Pons, M. C. H. Wong, D. Descamps, S. Petit, H. Ruf, N. Thire, A. Ferre, J. Suarez, J. Higuet, B. E. Schmidt, A. F. Alharbi, F. Legare, V. Blanchet, B. Fabre, S. Patchkovskii, O. Smirnova, Y. Mairesse, and V. R. Bhardwaj, “Probing molecular chirality on a sub-femtosecond timescale,” Nature Physics **11**, 654 (2015).
- [11] Matthias Dammasch, Martin Dörr, Ulli Eichmann, Ernst Lenz, and Wolfgang Sandner, “Relativistic laser-field-drift suppression of nonsequential multiple ionization,” Phys. Rev. A **64**, 061402 (2001).
- [12] Michael Klaiber, Enderalp Yakaboylu, Heiko Bauke, Karen Z. Hatsagortsyan, and Christoph H. Keitel, “Under-the-barrier dynamics in laser-induced relativistic tunneling,” Phys. Rev. Lett. **110**, 153004 (2013).
- [13] M. Klaiber, K. Z. Hatsagortsyan, J. Wu, S. S. Luo, P. Grugan, and B. C. Walker, “Limits of strong field rescattering in the relativistic regime,” Phys. Rev. Lett. **118**, 093001 (2017).
- [14] S. Palaniyappan, A. DiChiara, E. Chowdhury, A. Falkowski, G. Ongadi, E. L. Huskins, and B. C. Walker, “Ultrastrong field ionization of Ne<sup>n+</sup> ( $n \leq 8$ ): Rescattering and the role of the magnetic field,” Phys. Rev. Lett. **94**, 243003 (2005).
- [15] Morten Førre and Aleksander Skjerlie Simonsen, “Nondipole ionization dynamics in atoms induced by intense XUV laser fields,” Phys. Rev. A **90**, 053411 (2014).
- [16] U. Eichmann, T. Nubbemeyer, H. Rottke, and W. Sandner, “Acceleration of neutral atoms in strong short-pulse laser fields,” Nature **461**, 1261 (2009).
- [17] S. Eilzer, H. Zimmermann, and U. Eichmann, “Strong-field Kapitza-Dirac scattering of neutral atoms,” Phys. Rev. Lett. **112**, 113001 (2014).
- [18] H. Zimmermann and U. Eichmann, “Atomic excitation and acceleration in strong laser fields,” Physica Scripta **91**, 104002 (2016).
- [19] Qi Wei, Pingxiao Wang, Sabre Kais, and Dudley Herschbach, “Pursuit of the Kramers-Henneberger atom,” Chem. Phys. Lett. **683**, 240–246 (2017).
- [20] D. Schulze, A. Thakur, A.S. Moskalenko, and J. Berakdar, “Accelerating, guiding, and sub-wavelength trapping of neutral atoms with tailored optical vortices,” Ann. Phys. **529**, 1600379 (2017).
- [21] H. Zimmermann, S. Meise, A. Khujakulov, A. Magaña, A. Saenz, and U. Eichmann, “Limit on excitation and stabilization of atoms in intense optical laser fields,” Phys. Rev. Lett. **120**, 123202 (2018).
- [22] T. Nubbemeyer, K. Gorling, A. Saenz, U. Eichmann, and W. Sandner, “Strong-field tunneling without ionization,” Phys. Rev. Lett. **101**, 233001 (2008).
- [23] U. Eichmann, A. Saenz, S. Eilzer, T. Nubbemeyer, and W. Sandner, “Observing Rydberg atoms to survive intense laser fields,” Phys. Rev. Lett. **110**, 203002 (2013).
- [24] M. P. de Boer and H. G. Muller, “Observation of large populations in excited states after short-pulse multiphoton ionization,” Phys. Rev. Lett. **68**, 2747–2750 (1992).
- [25] R. R. Jones, D. W. Schumacher, and P. H. Bucksbaum, “Population trapping in Kr and Xe in intense laser fields,” Phys. Rev. A **47**, R49–R52 (1993).
- [26] Benjamin Wolter, Christoph Lemell, Matthias Baudisch, Michael G. Pullen, Xiao-Min Tong, Michaël Hemmer, Arne Senftleben, Claus Dieter Schröter, Joachim Ullrich, Robert Moshammer, Jens Biegert, and Joachim Burgdörfer, “Formation of very-low-energy states crossing the ionization threshold of argon atoms in strong mid-infrared fields,” Phys. Rev. A **90**, 063424 (2014).
- [27] B. Piraux, F. Mota-Furtado, P. F. O’Mahony, A. Galstyan, and Yu. V. Popov, “Excitation of Rydberg wave packets in the tunneling regime,” Phys. Rev. A **96**, 043403 (2017).
- [28] L. Ortmann, C. Hofmann, and A. S. Landsman, “Dependence of Rydberg-state creation by strong-field ionization on laser intensity,” Phys. Rev. A **98**, 033415 (2018).
- [29] Shaohao Chen, Xiang Gao, Jiaming Li, Andreas Becker, and Agnieszka Jaroní-Becker, “Application of a numerical-basis-state method to strong-field excitation and ionization of hydrogen atoms,” Phys. Rev. A **86**, 013410 (2012).
- [30] Qianguang Li, Xiao-Min Tong, Toru Morishita, Hui Wei,

and C. D. Lin, "Fine structures in the intensity dependence of excitation and ionization probabilities of hydrogen atoms in intense 800-nm laser pulses," *Phys. Rev. A* **89**, 023421 (2014).

[31] H. Zimmermann, S. Patchkovskii, M. Ivanov, and U. Eichmann, "Unified time and frequency picture of ultrafast atomic excitation in strong laser fields," *Phys. Rev. Lett.* **118**, 013003 (2017).

[32] M Gavrila, "Atomic stabilization in superintense laser fields," *J. Phys. B* **35**, R147–R193 (2002).

[33] AM Popov, OV Tikhonova, and EA Volkova, "Strong-field atomic stabilization: numerical simulation and analytical modelling," *J. Phys. B* **36**, R125–R165 (2003).

[34] Felipe Morales, Maria Richter, Serguei Patchkovskii, and Olga Smirnova, "Imaging the Kramers-Henneberger atom," *Proc. Natl. Acad. Sci. USA* **108**, 16906–16911 (2011).

[35] AM Popov, OV Tikhonova, and EA Volkova, "Applicability of the Kramers-Henneberger approximation in the theory of strong-field ionization," *J. Phys. B* **32**, 3331–3345 (1999).

[36] JC Wells, I Simbotin, and M Gavrila, "Physical reality of light-induced atomic states," *Phys. Rev. Lett.* **80**, 3479–3482 (1998).

[37] A. M. Popov, O. V. Tikhonova, and E. A. Volkova, "Different regimes of strong-field dynamics of atoms in intense low-frequency laser pulses," *J. Modern Opt.* **58**, 1195–1205 (2011).

[38] M. Gavrila, I. Simbotin, and M. Stroe, "Low-frequency atomic stabilization and dichotomy in superintense laser fields from the high-intensity high-frequency Floquet theory," *Phys. Rev. A* **78**, 033404 (2008).

[39] I Simbotin, M Stroe, and M Gavrila, "Quasistationary stabilization and atomic dichotomy in superintense low-frequency fields," *Laser Phys.* **14**, 482–491 (2004).

[40] See Supplemental Material at [URL to be inserted by publisher].

[41] Dror Shafir, Hadas Soifer, Barry D. Bruner, Michal Dagan, Yann Mairesse, Serguei Patchkovskii, Misha Yu. Ivanov, Olga Smirnova, and Nirit Dudovich, "Resolving the time when an electron exits a tunnelling barrier," *Nature* **485**, 343–346 (2012).

[42] Barry D. Bruner, Hadas Soifer, Dror Shafir, Valeria Serebrenko, Olga Smirnova, and Nirit Dudovich, "Multidimensional high harmonic spectroscopy," *J. Phys. B* **48**, 174006 (2015).

# Dissecting strong-field excitation dynamics with atomic-momentum spectroscopy

A.W. Bray,<sup>1,\*</sup> U. Eichmann,<sup>2,†</sup> and S. Patchkovskii<sup>2,‡</sup>

<sup>1</sup>*Australian National University, Canberra*

<sup>2</sup>*Max-Born-Institute, Berlin, Germany*

(Dated: December 5, 2021)

## SUPPLEMENTAL MATERIAL

### Computational details

We apply the parabolic trapping potential  $u(\vec{R}) = kR^2/2$  with  $k = 10^{-4}$ . We include four c.m. eigenstates: the initially-populated ground state corresponds to a Gaussian wavepacket of  $\approx 2.5 a_0$  width, and the three singly-excited harmonic vibrational modes, one along each Cartesian direction. For simulations discussed below and in the main text, electronic populations associated with the excited c.m. states do not exceed  $7 \times 10^{-3}$ . The electronic wavefunction is discretized on a uniform, Cartesian-product grid extending to  $\pm 78.6 a_0$  in the  $X$  and  $Y$  directions, and to  $\pm 152.1 a_0$  along  $Z$  (the laser polarization direction). Uniform grid spacing is  $0.35 a_0$ . A transmission-free absorbing boundary[1] is applied starting  $9.4 a_0$  from all grid edges.

The laser beam propagates toward the positive  $X$  direction. We model the vector-potential of the beam by a paraxial TEM<sub>00</sub> mode, including the lowest-order longitudinal correction[2]:

$$A_z = A_0 f \left( t - \frac{x}{c} \right) \Re \left[ \left( 1 - \frac{ix}{z_R} \right)^{-1} e^\Phi \right] \quad (\text{S1})$$

$$A_x = A_0 f \left( t - \frac{x}{c} \right) \Re \left[ \frac{iz}{z_R} \left( 1 - \frac{ix}{z_R} \right)^{-2} e^\Phi \right] \quad (\text{S2})$$

$$\Phi = -ikx + i\omega t + i\varphi_0 - \frac{r^2}{w_0^2} \left( 1 - \frac{ix}{z_R} \right)^{-1} \quad (\text{S3})$$

where the beam waist  $w_0 = 30236 a_0$ , Rayleigh range  $z_R = \pi w_0/\lambda$ ,  $\lambda = 2\pi c/\omega$  is the wavelength,  $k = 2\pi/\lambda$  is the wavevector, and  $c \approx 137$  is the speed of light. Unless noted otherwise, the slowly-varying envelope  $f(t - x/c)$  is a truncated Gaussian[3] with the FWHM of 220 ( $\approx 5.32$  fs) and baseline duration of 800 ( $\approx 19.4$  fs). The carrier frequency  $\omega = 0.057$ , corresponding to  $\lambda \approx 799$  nm. The peak vector-potential at the focal-spot centre is 2.9615, corresponding to a peak field intensity of  $\approx 1$  PW cm<sup>-2</sup>. Eqs. (8) are integrated using the leap-frog propagator with the time step of 0.005. Using the 4th-order Runge-Kutta propagator leads to numerically equivalent results. We analyze the results by projecting the final wavefunctions onto hydrogenic states (Eq. (14)). Our simulation volume is sufficient to resolve Rydberg states up to the principal quantum num-

ber  $n = 6$ . We verified that a further increase in the simulation volume does not affect these results.

### Treatment for the general masses and charges

The minimal-coupling non-relativistic Hamiltonian for two particles is given by:

$$\hat{H} = \frac{1}{2m_1} \left( \hat{p}_1 - q_1 \vec{A}(\vec{r}_1, t) \right)^2 + \frac{1}{2m_2} \left( \hat{p}_2 - q_2 \vec{A}(\vec{r}_2, t) \right)^2 + v(\vec{\chi}) + u(\vec{R}) \quad (\text{S4})$$

where  $m_i$ ,  $q_i$ , and  $\hat{p}_i$ ,  $i = 1, 2$  are respectively the mass, charge, and momentum operator for particles 1 and 2. Using the standard c.m. variable substitution (see the main text), we obtain, for the transverse field  $\vec{A}$ :

$$\begin{aligned} \hat{H} = & \frac{1}{2\mu} \hat{p}_\chi^2 - \left( \frac{1}{m_1} \vec{A}_1 - \frac{1}{m_2} \vec{A}_2 \right) \cdot \hat{p}_\chi + \frac{1}{2m_1} A_1^2 \\ & + \frac{1}{2m_2} A_2^2 + v(\vec{\chi}) + \frac{1}{2M} \hat{p}_R^2 - \frac{1}{M} \left( \vec{A}_1 + \vec{A}_2 \right) \cdot \hat{p}_R \\ & + u(\vec{R}) - \frac{1}{\mu} R_a \left( \vec{A}_1^{(a)} + \vec{A}_2^{(a)} \right) \cdot \hat{p}_\chi \\ & - R_a \left( \frac{1}{m_2} \vec{A}_1^{(a)} - \frac{1}{m_1} \vec{A}_2^{(a)} \right) \cdot \hat{p}_R \\ & + \frac{1}{\mu} R_a \left( \vec{A}_1 \cdot \vec{A}_1^{(a)} - \vec{A}_2 \cdot \vec{A}_2^{(a)} \right) \\ & + \frac{1}{2\mu} R_a R_b \left( \frac{M}{m_2} \vec{A}_1^{(a)} \cdot \vec{A}_1^{(b)} + \frac{M}{m_1} \vec{A}_2^{(a)} \cdot \vec{A}_2^{(b)} \right) \end{aligned} \quad (\text{S5})$$

where summation over indices  $a$  and  $b$  is implied, and quantities  $\vec{A}_i$  and  $\vec{A}_i^{(a)}$  ( $i = 1, 2$ ;  $a = x, y, z$ ) are given by:

$$\vec{A}_1(\vec{\chi}) = q_1 \vec{A} \left( \frac{m_2}{M} \vec{\chi} \right) \quad (\text{S6})$$

$$\vec{A}_2(\vec{\chi}) = q_2 \vec{A} \left( -\frac{m_1}{M} \vec{\chi} \right) \quad (\text{S7})$$

$$\vec{A}_i^{(a)}(\vec{\chi}) = \frac{\partial}{\partial \chi_a} \vec{A}_i(\vec{\chi}). \quad (\text{S8})$$

In deriving Eq. (S5) we further assumed that  $\vec{R}$  is small, so that the higher-order terms can be neglected in Eq. (13).

Equation (S5) has been implemented numerically within the Ansatz of the Eq. (7), and is propagated numerically for the same grids and trap parameters as the Eq. (8) in the main text. The propagation cost is  $\approx 5 \times$

that of Eq. (8). For atomic hydrogen, the results on the scale of the graphs shown in the main text and the supplementary material are indistinguishable from those of the approximate Eq. (8).

### Additional results

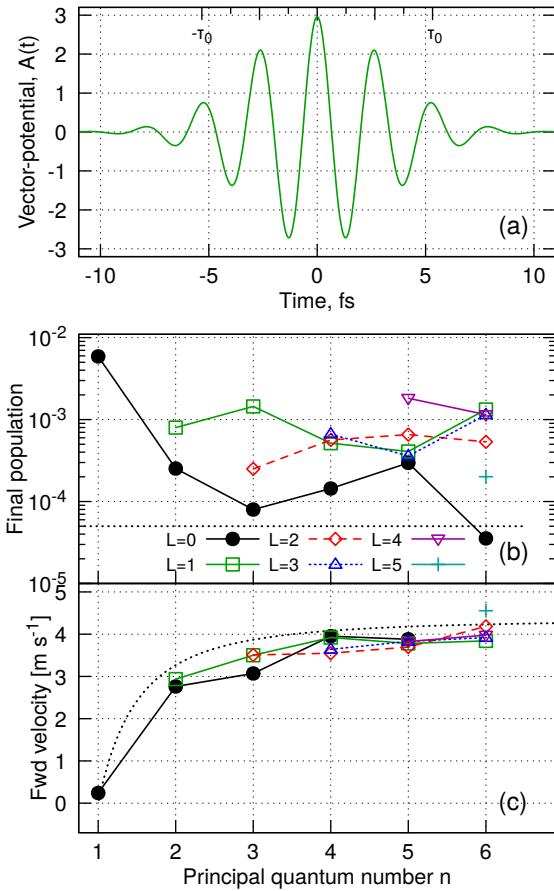


FIG. S1. (Color online) Hydrogen atom initially at the centre of the focal spot. Local peak intensity  $1 \text{ PW cm}^{-2}$ . Also see Fig. S2 caption.

We begin by briefly examining the dynamics of a hydrogen atom at the centre of the focal spot (Fig. S1), where the laser field remains essentially a planewave. At  $1 \text{ PW cm}^{-2}$  local peak intensity, ionization is in the saturation regime. Only 0.6% of the hydrogen atoms remain in the  $1s$  ground state. Additionally, approximately 1.3% of the atoms are excited to Rydberg states with  $n \leq 6$ . We further estimate that at least 2% of the atoms are left in Rydberg states with  $n \geq 7$ . Most of the excited states possess magnetic quantum number  $m=0$ , same as the initial state. The total final population of  $m=\pm 1$  ( $m=\pm 2$ ) manifolds is  $\approx 5.8 \times 10^{-6}$  ( $\approx 1.1 \times 10^{-9}$ ). Similar low  $m \neq 0$  excitation probabilities are seen for most other field parameters considered below. Due to their

low population, we do not consider  $m \neq 0$  states any further. The individual excitation probabilities and final c.m. velocities are collected in Fig. S1. These results are qualitatively similar to those at the half-waist position, discussed below and in the main text.

The final populations of the  $m=0$  states are illustrated in Fig. S1b. The corresponding c.m. velocities in the propagation direction are shown in Fig. S1c. We find that the calculated velocities become erratic for very low final populations, which amplify the inevitable numerical noise in the solutions (see Eq. (15)). As a result, we choose to disregard the calculated c.m. velocities when the corresponding population drops below  $5 \times 10^{-5}$  (e.g. for the  $6s$  state in Fig. S1c). The net number of photons absorbed from the laser field is zero for the  $1s$  ground state, which consequently acquires no forward velocity. For all other states in Fig. S1c, the final forward velocity is in the range of  $2.8 \text{ m s}^{-1}$  ( $2s$ ) to  $4.6 \text{ m s}^{-1}$  ( $6h$ ). These values are consistent with the momentum transfer due to the radiation pressure (Eq. (16)), and carry no information on the internal dynamics of the system.

We now turn to positions away from the centre of the focal spot, where the laser field is no longer well-approximated by a planewave. As discussed in the main text, the maximum of the spatial gradient of the ponderomotive potential is found on a ring of the radius  $w_0/2$  around the focal spot, normal to the beam propagation direction. We begin by choosing the point displaced in the  $y$  direction, perpendicular to both the propagation and polarization directions. The non-paraxial corrections of Eq. (S2) vanish in the vicinity of this point. The local peak intensity of the field is  $\approx 607 \text{ TW cm}^{-2}$ . The ionization remains in the saturation regime, with  $\approx 10\%$  of the population surviving in the ground state after the pulse. The numerical results at this point are illustrated in Fig. S2. The final populations of the Rydberg states are of a similar overall magnitude to those found at the beam centre, with  $\approx 1.4\%$  left in Rydberg states with  $n \leq 6$ , and  $\geq 3\%$  in states with  $n \geq 7$ .

The forward velocities at the half-waist position (Fig S2c) follow a trend similar to the beam centre, and are consistent with the radiation-pressure effects. The forward velocity is insensitive to the small transverse intensity gradient. Repeating the calculation with a planewave field at the  $607 \text{ TW cm}^{-2}$  peak intensity yields results visually identical to Fig. S2c.

From Eq. (17), we expect the transverse, ponderomotive acceleration to yield the maximum velocity when a Rydberg state is formed early within the laser pulse ( $t_b \rightarrow -\infty$ ). This sets the upper bound on the final transverse velocity a state with a free-electron-like polarizability could reach. For the field parameters in Fig. S2, the limit is  $24.6 \text{ m s}^{-1}$ , indicated by the dotted line in panel (d). This limit is exceeded by the  $3p$  and  $5d$  states, indicating that the magnitude of their effective polarizability exceeds the free-electron value ( $\approx -308$  at  $\omega = 0.057$ ). In

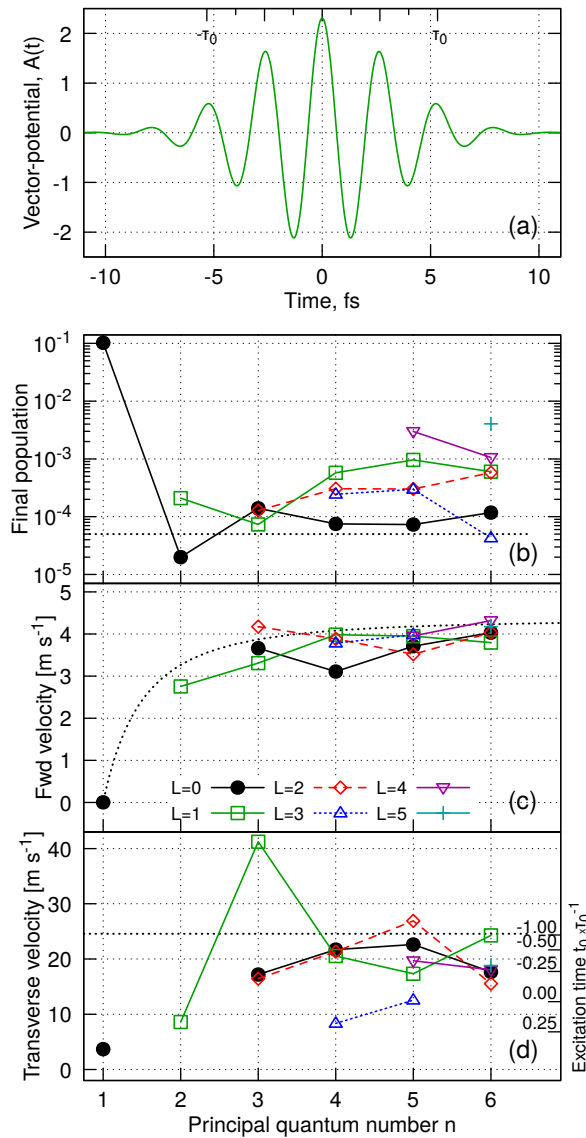


FIG. S2. (Color online) Hydrogen atom initially at the beam half-waist (the Cartesian position  $(0, w_0/2, 0)$ ; no spatial averaging). Local peak intensity  $\approx 607 \text{ TW cm}^{-2}$ . (a) Vector-potential at the initial position as a function of time. The upper horizontal axis gives the fraction of the pulse duration  $\tau_0$ . (b) Population of the individual  $m=0$  bound states after the end of the pulse. Horizontal dotted line indicates the acceptance cut-off (see text). (c) Final c.m. velocity in the beam propagation direction in meters per second (1 a.u.  $\approx 2.19 \times 10^6 \text{ m s}^{-1}$ ). The dotted line indicates the  $\Delta E/Mc$  contribution to the final velocity expected from the field momentum transfer. (d) Final c.m. velocity in the outward transverse direction. The right vertical axis gives the time when a particle with free-electron polarizability needs to enter the field to reach the observed transverse velocity (Eq. (17)). Final velocities above the dotted horizontal line cannot be reached by a free electron (see text). The connecting lines in panels (b-d) are only a guide for the eye.

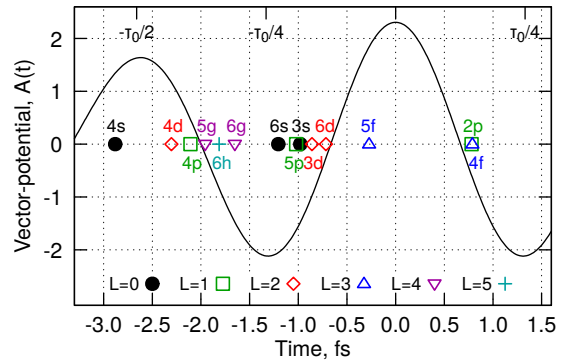


FIG. S3. (Color online) Reconstructed excitation times for the c.m. velocity spectra in Fig. S2 (see text). No excitation times can be assigned for the  $3p$ ,  $5s$ ,  $5d$ , and  $6p$  states, which are affected by resonances, or for the  $1s$  ground state. The solid line is the vector-potential from Fig. S2.

the case of the  $3p$  state, which reaches the final transverse velocity of  $41 \text{ m s}^{-1}$ , we speculate that the likely reason is a 1-photon resonance with the Stark-shifted  $2s$  state ( $1.9 \text{ eV}$  away in the absence of the field). The resonance depleted the  $2s$  state (final population of  $1.9 \times 10^{-5}$ ), while simultaneously increasing the effective polarizability and the acceleration of the  $3p$  state. Because strong-field resonances are highly-sensitive to the local peak intensity, we anticipate such resonances to be washed out by the spatial averaging (see below and in the main text).

We can now invert Eq. (17) to extract the time estimate  $t_b$ . We assume that the frequency-dependent polarizability of the final state is  $-\omega_0^{-2}$  ( $\approx -308$ ). Away from resonances, this estimation becomes progressively more accurate for higher Rydberg states. The resulting excitation-time reconstruction is shown in Fig. S3.

In the volume-averaged simulation (Fig. 1 of the main text),  $t_b$  can be consistently assigned for all final states. Because suppression of resonances appears to be important for a successful reconstruction of the excitation time, all subsequent results use volume-averaging protocol similar to that in Fig. 1 ( $\pm 648 a_0$  along the maximum intensity-gradient direction, covering  $\approx 2$  channel closings).

Up to now, we have considered a short, 2-cycle pulse with cosine CEP for the vector-potential. It is important to establish that the reconstruction is applicable to other pulse phases, longer pulses, and for the more realistic, non-paraxial tightly-focussed beam models.

The results for the pulse with sine vector-potential CEP phase (all other parameters remain the same as in Fig. 1) are shown in Fig. S4. This pulse leaves  $\approx 9.5\%$  of the atoms in the  $1s$  ground state,  $\approx 2.5\%$  in Rydberg states with  $n \leq 6$ , and at least  $2.5\%$  in higher Rydberg states. The final transverse velocity of the  $1s$  ground state is  $\approx 3.3 \text{ m s}^{-1}$ . The reconstructed excitation times are shown in Fig. S5. These results are qualitatively sim-

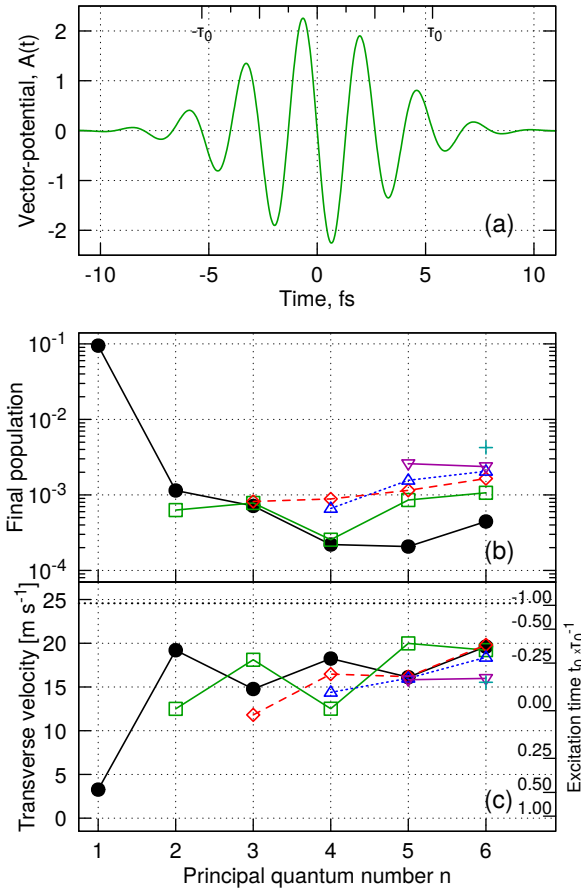


FIG. S4. (Color online) Same as Fig. 1, but for the vector-potential CEP of  $\pi/2$ . The results are an equally-weighted average over the initial positions are within  $\pm 648 a_0$  of the beam half-waist position along  $y$ . Also see captions of Figs. 1 and S2.

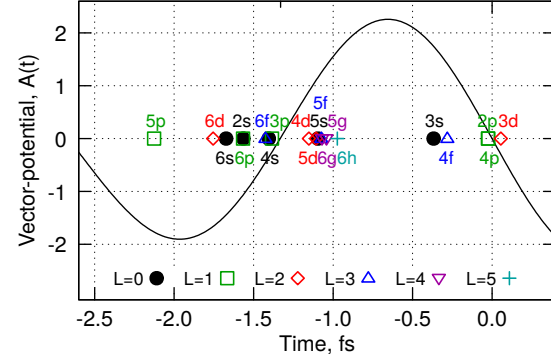


FIG. S5. (Color online) Reconstructed excitation times for the data in Fig. S4. Also see Fig. 2 caption.

ilar to Figs. 1,2 of the main text: The excitation is most likely to occur at a small number of times, close to the zeros of the vector-potential (peaks of the electric field).

The results for the 440 ( $\approx 10.64$  fs) FWHM, cosine CEP pulse (all other parameters same as in Fig. 1) are shown in Fig. S6. The longer pulse leads to a stronger de-

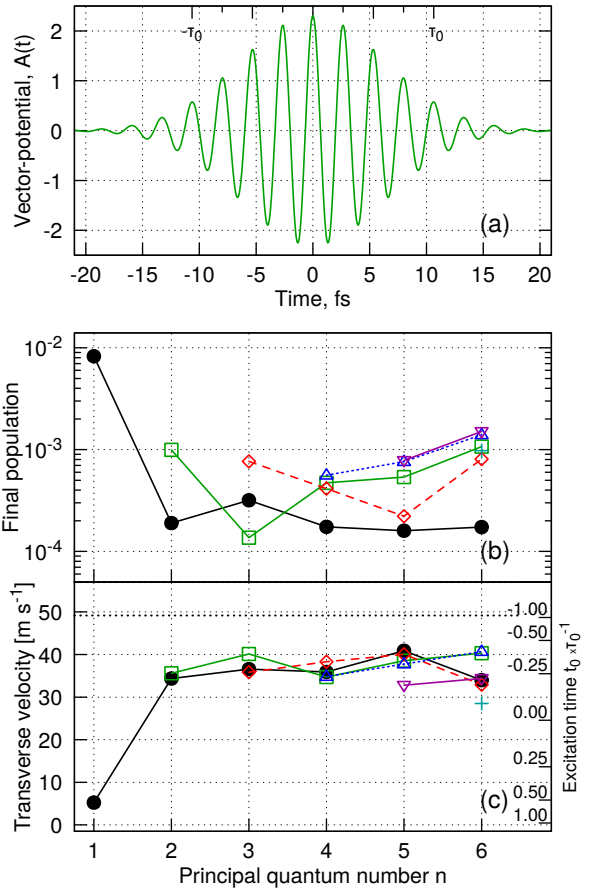


FIG. S6. (Color online) Same as Fig. 1, but for the pulse duration of 440 ( $\approx 10.64$  fs). The results are an equally-weighted average over the initial positions are within  $\pm 648 a_0$  of the beam half-waist position along  $y$ . Also see caption of Fig. 1.

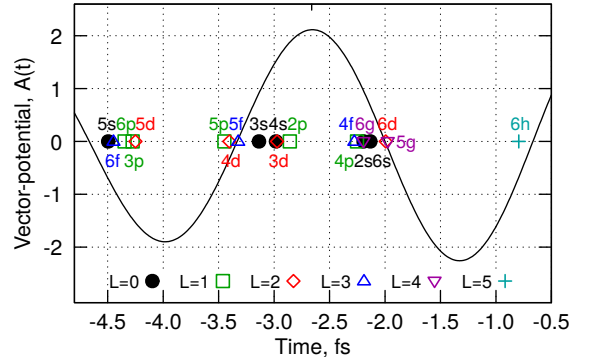


FIG. S7. (Color online) Reconstructed excitation times for the data in Fig. S6. Also see Fig. 2 caption.

pletion, with only 0.8% of the atoms surviving in the  $1s$  ground state. The fraction of the Rydberg states remains essentially unchanged, with 1.2% of the atoms remaining in  $m = 0$  states with  $n \leq 6$ , and at least 1.3% in higher states. Due to the longer pulse duration, the ground state now reaches the higher transverse velocity of  $\approx 5.2 \text{ m s}^{-1}$ , 11% of the free electron limit ( $49.1 \text{ m s}^{-1}$ ). The longer

pulse significantly increases the probability of magnetic transitions, with  $\approx 0.7\%$  ( $0.08\%$ ) of the Rydberg states left with  $m = \pm 1$  ( $\pm 2$ ). The probability of populating  $m \neq 0$  states increases for higher values of the principal quantum numbers. Our analysis still concentrates on the  $m = 0$  states, which dominate the  $n \leq 6$  population. The reconstructed excitation times are shown in Fig. S7. These values follow the same pattern as before, with a small number of likely excitation times, occurring well before the peak of the envelope.

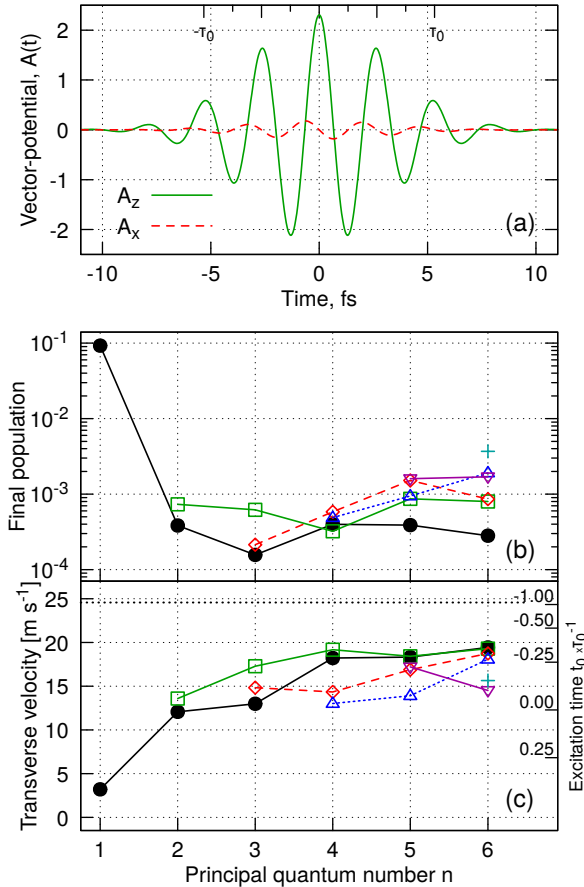


FIG. S8. (Color online) Same as Fig. 1, but for the initial position displaced along the laser polarization ( $z$ ) direction  $(0, 0, w_0/2 \pm 648)$ . Non-paraxial effects are no longer negligible for this beam position, see Eq. (S2). (a) Vector-potential in the along the polarization (green solid line) and propagation (red dashed line) directions. Also see caption of Fig. 1.

Our final test case uses the same pulse and beam parameters as Fig. 1, but considers an initial position displaced along the field polarization direction  $z$ . Again, the numerical results are averaged along a  $\pm 648 a_0$  line in the maximum intensity-gradient direction ( $z$ ). The ground-state survival probability is unchanged at 9%, compared to Fig. 1. The excitation probabilities remain similar, at  $\approx 1.8\%$  for  $n \leq 6$  and at least 1.7% for higher Rydberg states with  $m=0$ . At the same time, the laser field now has a component in the propagation direction, which en-

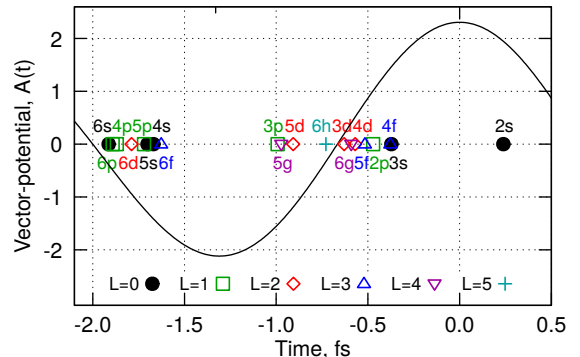


FIG. S9. (Color online) Reconstructed excitation times for the data in Fig. S8. Also see Fig. 2 caption.

ables efficient excitation of  $m \neq 0$  states. The  $n \leq 6$ ,  $m = \pm 1$  states now account for  $\approx 0.1\%$  of the initially-present atoms. The transverse velocity of the  $1s$  ground state remains unchanged at  $\approx 3.2 \text{ m s}^{-1}$ . Finally, the reconstructed excitation times, shown in Fig. S9, follow the same pattern as before.

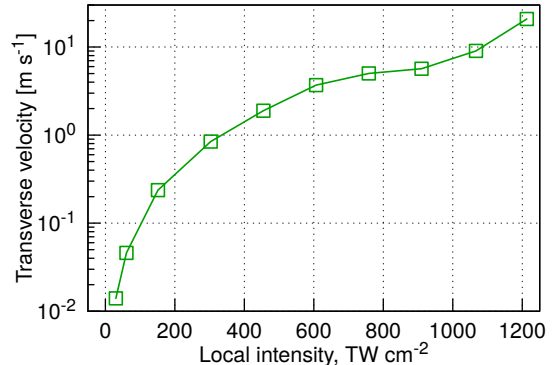


FIG. S10. (Color online) Final outward transverse velocity for the hydrogen  $1s$  ground state as a function of the peak intensity at the centre of the beam. Pulse parameters and the initial conditions are given in the Fig. 3 caption.

\* alexander.bray@anu.edu.au

† eichmann@mbi-berlin.de

‡ sergeui.patchkovskii@mbi-berlin.de

- [1] David E. Manolopoulos, “Derivation and reflection properties of a transmission-free absorbing potential,” *J. Chem. Phys.* **117**, 9552–9559 (2002).
- [2] Melvin Lax, William H. Louisell, and William B. McKnight, “From Maxwell to paraxial wave optics,” *Phys. Rev. A* **11**, 1365–1370 (1975).
- [3] Serguei Patchkovskii and H. G. Muller, “Simple, accurate, and efficient implementation of 1-electron atomic time-dependent Schrodinger equation in spherical coordinates,” *Comp. Phys. Comm.* **199**, 153–169 (2016).